Supporting Information

Multi-electron/ion conduction channels enabling high-performance flexible supercapacitors

Fan Zeng,[a] Xianyin Song,*[a] Jing Liang,[b] Xingang Zhang,[ac] Xuefeng Sha,[a] Xueli Wu,[a] Hongtao Zhou,[a] Zhi Liu,[c] Wei Wu,*[b] and Changzhong Jiang*[a]

[a] College of Materials Science and Engineering, Hunan University, Changsha 410082, China. E-mail: songxy@hnu.edu.cn, czjiang@hnu.edu.cn

[b] Laboratory of Printable Functional Materials and Printed Electronics, School of Printing and Packaging, Wuhan University, Wuhan 430072, China. E-mail: weiwu@whu.edu.cn

[c] Key Laboratory of Low-Dimensional Quantum Structures and Quantum Control of Ministry of Education, Key Laboratory for Matter Microstructure and Function of Hunan Province, Department of Physics and Synergetic Innovation Center for Quantum Effects and Applications, Hunan Normal University, Changsha 410081, China.

Experimental Section

Materials

Nickel nitrate hexahydrate ($Ni(NO_3)_2 \cdot 6H_2O$), N-methylpyrrolidone (NMP), potassium hydroxide (KOH), Iron nitrate nonahydrate ($Fe(NO_3)_3 \cdot 9H_2O$), and acetylene black are purchased from Sinopharm Chemical Reagent Co. Ltd. Polyvinylidene fluoride (PVDF, HSV900) is manufactured by Arkema Kynar. Graphene powders are purchased from Shanghai Aladdin Biochemical Technology Co. Ltd. Degreasing cotton is purchased from Nanchang Chaoyang Medical and Health Products Co., Ltd. LA133 binder, acetylene black and silver paste are purchased as the binder, conductive additives, and current collector, respectively.

Preparation of Fe_2O_3/CF, NiO/CF and Fe_2O_3/CF@Gs, NiO/CF@Gs inks

3D hierarchical porous carbon fibers (CF) were prepared by high-temperature carbonization of degreasing cotton at 1000 ℃ for 2 hours under argon atmosphere. After cooling to room temperature, the obtained CF were grinded and immerged into certain concentration of $Fe(NO_3)_3$ or $Ni(NO_3)_2$ solution and stirring intensively. Then, after centrifugation and drying, the Fe_2O_3/CF is fabricated by annealing the intermediate $Fe(NO_3)_3$/CF powers at 450 ℃ for 1 hour under an argon protective atmosphere following the chemical equation of $4Fe(NO_3)_3 \rightarrow 2Fe_2O_3 + 12NO_2\uparrow + 3O_2\uparrow$, and NiO/CF is obtained at the same condition following the chemical equation of $2Ni(NO_3)_2 \rightarrow 2NiO + 4NO_2\uparrow + O_2\uparrow$. The other composite electrodes, like Co_3O_4/CF, MnO_2/CF and MoO_3/CF, were fabricated by the same procedure. Pure NiO, Fe_2O_3, Co_3O_4, MnO_2 and MoO_3 samples were obtained by direct heat treatment of the

corresponding inorganic metal salts at the same temperatures. The composition of Fe_2O_3/CF@Gs (NiO/CF@Gs) inks included the Fe_2O_3/CF (NiO/CF), LA133 binder, acetylene black and graphene sheets (Gs), which were dispersed into deionized (DI) water under the mass ratio of 7 : 1 : 1 : 1. In the prepared of ink, the solid content of Fe_2O_3/CF@Gs (NiO/CF@Gs) material was ca. 22 wt%. The Fe_2O_3 (NiO) and Fe_2O_3/CF (NiO/CF) ink is formed by the same procedures without graphene. And the composition of Fe_2O_3/CF (NiO/CF, Fe_2O_3 and NiO) ink includes the Fe_2O_3/CF (NiO/CF, Fe_2O_3 and NiO) powder, acetylene black and LA133 binder, which were mixed in distilled water according the weight ratio of 75 : 15 : 10 based on our previous works.[1-3]

Fabrication of flexible supercapacitor

The customized flexible electrodes are manufactured by screen-printing method (200 mesh printing plate). Firstly, the silver pastes were printed on the PET flexible substrates and dried at 70 °C for 30 minutes. And then the Fe_2O_3/CF@Gs (NiO/CF@Gs) inks were overprinted on the silver layer at the squeegee speed of 2 cm s^{-1}. After dried at 70 °C for 30 minutes, the printed electrodes based on NiO/CF@Gs as positive and Fe_2O_3/CF@Gs as negative were prepared. The loading mass of dry reactive inks was 6～8 mg/cm^2 (Figure S9). Meanwhile, 4.0 g PVA and 2.4 g KOH were dissolved in 40 mL deionized water and stirred at 80 °C until the mixture became a clear solution to prepare the KOH/PVA gel electrolyte. Finally, KOH/PVA gel electrolytes were coated on the active electrode and a cellulose membrane was placed between the two electrodes to assemble a flexible supercapacitor.

Electrochemical test

Cyclic voltammetry (CV), galvanostatic charge/discharge (GCD), and electrochemical impedance spectroscopy (EIS) were collected on a CHI 760E electrochemical working station. In the three electrodes test, a Pt filament served as the counter electrode and Hg/HgO was used as the reference electrode in 6 M KOH, and the working electrode is fabricated by followed procedure. Firstly, the active material (Fe_2O_3/CF@Gs, Fe_2O_3/CF, Fe_2O_3 or NiO/CF@Gs, NiO/CF, NiO or CF), graphene, acetylene black and PVDF were mixed within NMP solvent according to the ink ratio above. Then, the mixed suspensions were dropped on the surface of foamed nickel and dried at 70 ℃ for 4 hours. Finally, the dried foamed nickel was pressed on 10 MPa for 30 seconds. The loading mass of active materials during the prepared working electrode was at approximate 2 mg/cm^2.

For two electrodes test, the printed NiO/CF@Gs electrode as the positive and Fe_2O_3/CF@Gs served as negative electrode. The cycling stability is tested by CT3001A battery test system.

The areal capacitance was computed by CV or GCD curves through Equation S1 and Equation S2:

$$C_S = \frac{1}{2 \times S \times v \times \Delta U} \int IdU \tag{1}$$

where v is scan rate (mV s^{-1}), S is area of supercapacitor, and ΔU is potential window.

$$C_S = \frac{I \times \Delta t}{S \times \Delta U} \tag{2}$$

where I is discharge current density, Δt is the discharge time, ΔU is the effective potential window, S is the effective active areal.

The energy density (E) and power density (P) could be calculated based on Equation S3 and Equation S4:

$$E = \frac{1}{2} C_S \times \Delta U^2 \tag{3}$$

$$P = \frac{E}{\Delta t} \tag{4}$$

where ΔU is the operational potential window (V), C_S is the areal capacitance, and Δt is the discharged time.

The capacitance of electrodes is calculated by CV curves based on the following Equation S5:

$$C_m = \frac{1}{2 \times m \times v \times \Delta U} \int I dU \tag{5}$$

where m is mass of active materials, ΔU is potential window, and v is scan rate (mV s^{-1}).

Material Characterization

The surface morphology and energy-dispersive X-ray (EDX) mapping were collected on a field-emission scanning electron microscopy (FE-SEM, TESCAN MIRA 3). The inner morphology and structure were characterized by the transmission electronic microscope (TEM, FEI Tecnai F20) operated at 200 kV. The crystal structures were measured by X-ray diffraction (XRD, Rigaku Miniflex 600) with Cu-Kα radiation (λ = 0.15418 nm). Raman spectroscopy was determined by commercial

Raman microscope (Horiba JY HR Evolution, France) with laser excited at 532 nm. The surface chemical states were investigated by X-ray photoelectron spectroscopy (XPS, Thermo Scientific K-Alpha) with Al K_α radiation (1486.6 eV), and the peak position was internally referenced to the C1s peak at 284.8 eV. Surface area and average pore diameter were obtained by nitrogen adsorption and desorption isotherm at 77 K by JW-BK200C analyzer. The rheological properties of inks are tested by a rheometer (HAAKE MARS60).

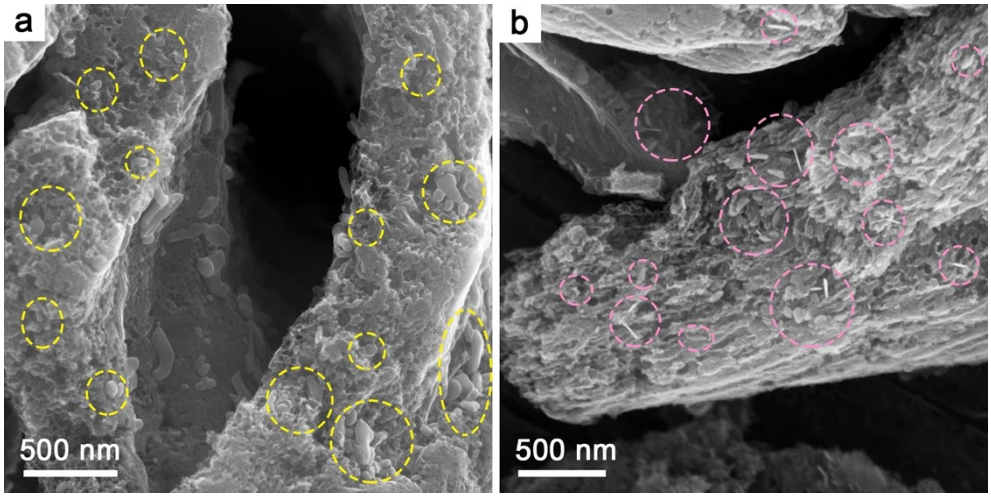

Figure S1. SEM images of metal-oxide and porous carbon fiber (CF) composite samples.

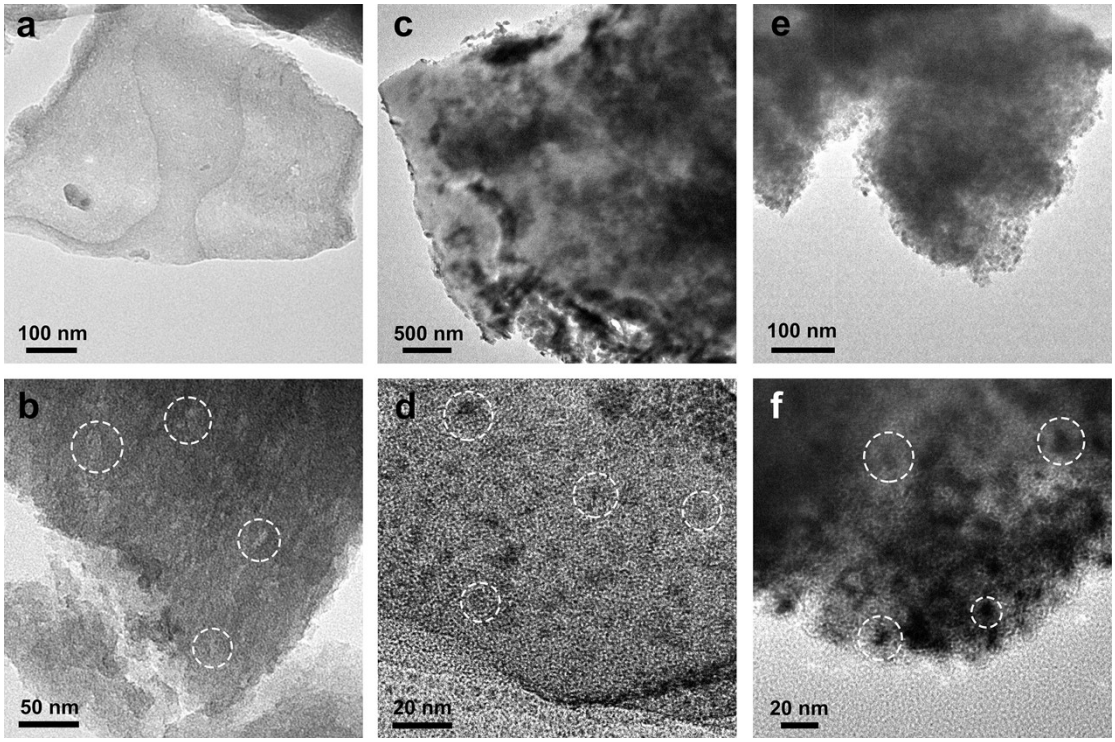

Figure S2. TEM images of (a, b) CF, (c, d) Fe_2O_3/CF and (e, f) NiO/CF composite samples.

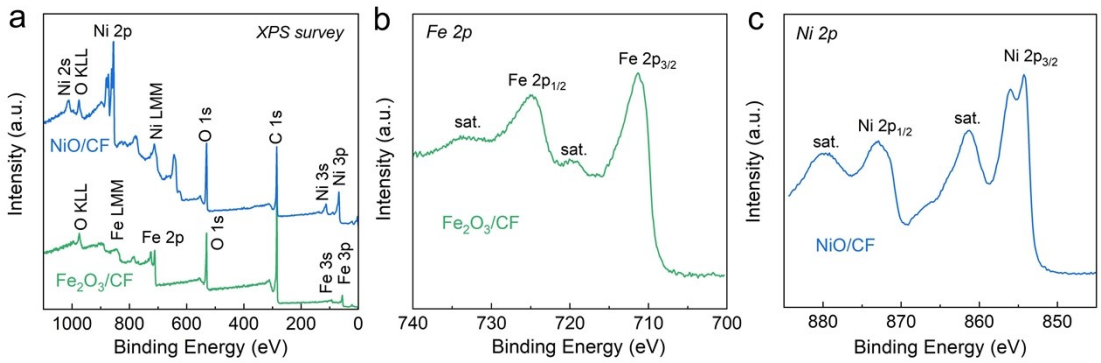

Figure S3. (a) The XPS survey spectra of Fe_2O_3/CF and NiO/CF samples. (b) XPS Fe 2p spectrum of Fe_2O_3/CF. (c) XPS Ni 2p spectrum of NiO/CF.

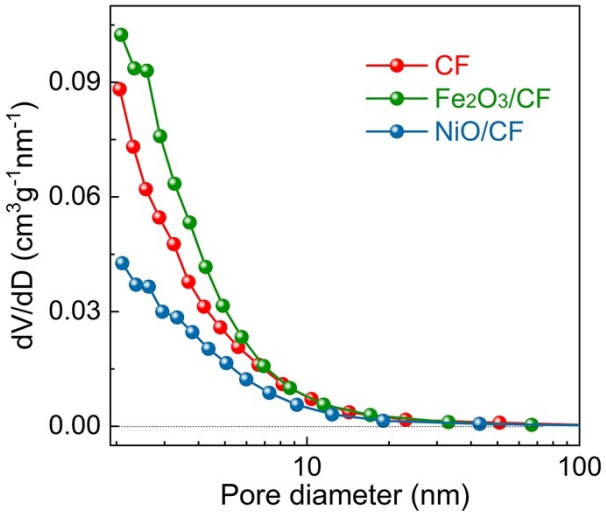

Figure S4. The mesoporous size (> 2 nm) distribution of CF, Fe_2O_3/CF and NiO/CF samples.

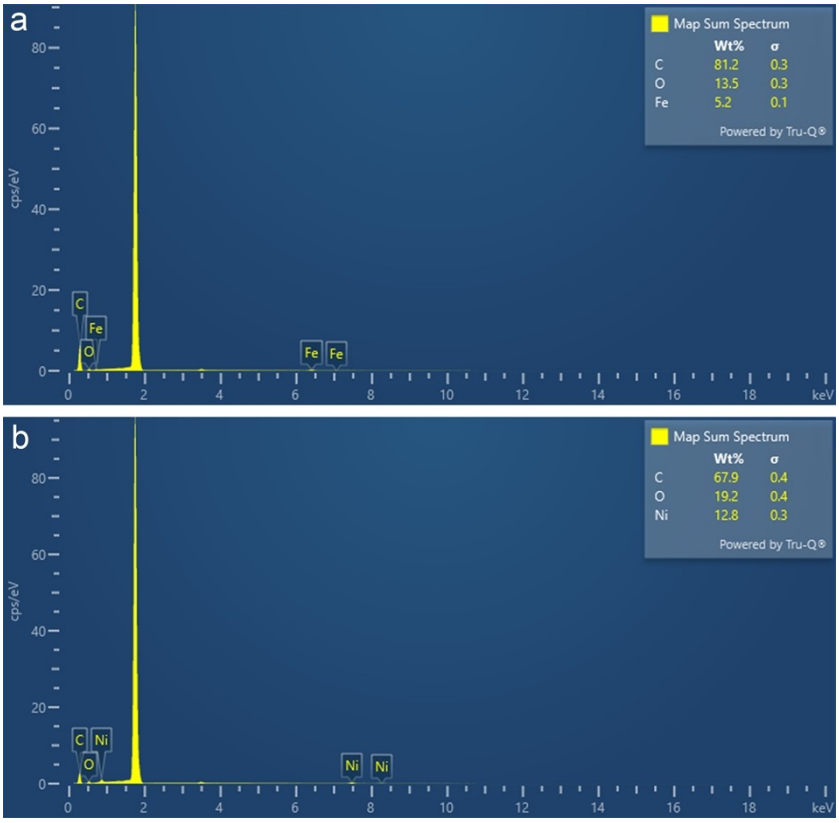

Figure S5. EDX spectra with quantitative atomic analysis of (a) Fe_2O_3/CF and (b) NiO/CF samples.

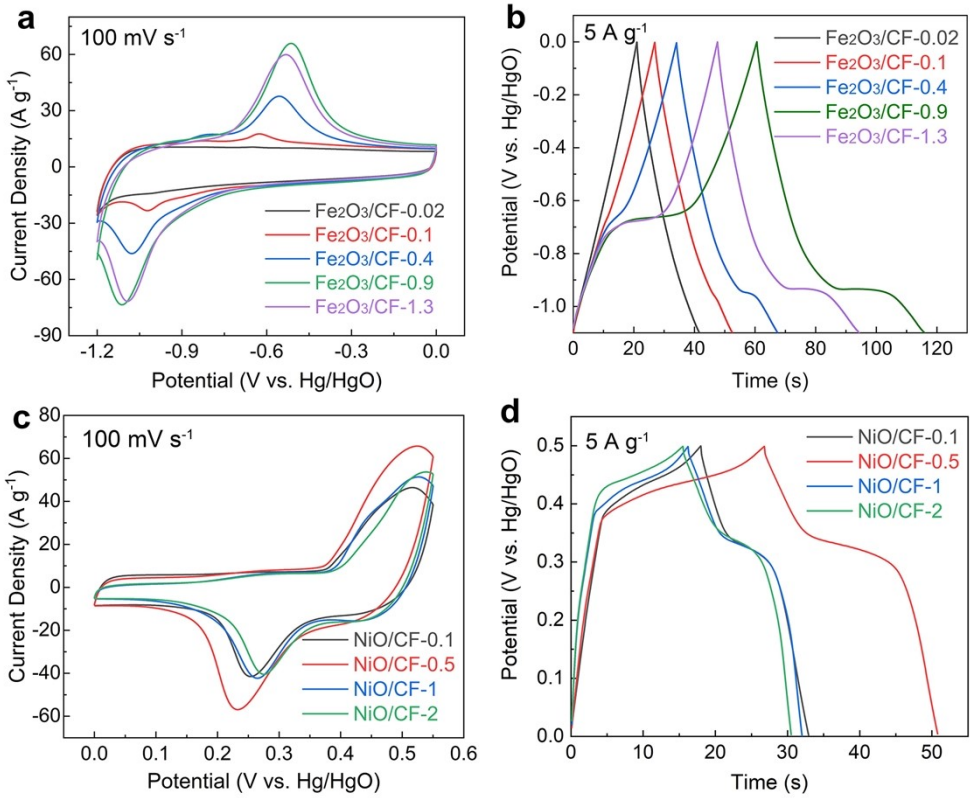

Figure S6. (a) CV curves of Fe_2O_3/CF-*x* at 100 mV s^{-1}. (b) GCD curves of Fe_2O_3/CF-*x* at 5 A g^{-1}. *x* denotes the concentration of $Fe(NO_3)_3 \cdot 9H_2O$ solution from 0.02~1.3 g mL^{-1}. (c) CV curves of NiO/CF-*y* at 100 mV s^{-1}. (d) GCD curves of NiO/CF-*y* at of 5 A g^{-1}. *y* denotes the concentration of $Ni(NO_3)_2 \cdot 6H_2O$ solution from 0.1~2 g mL^{-1}.

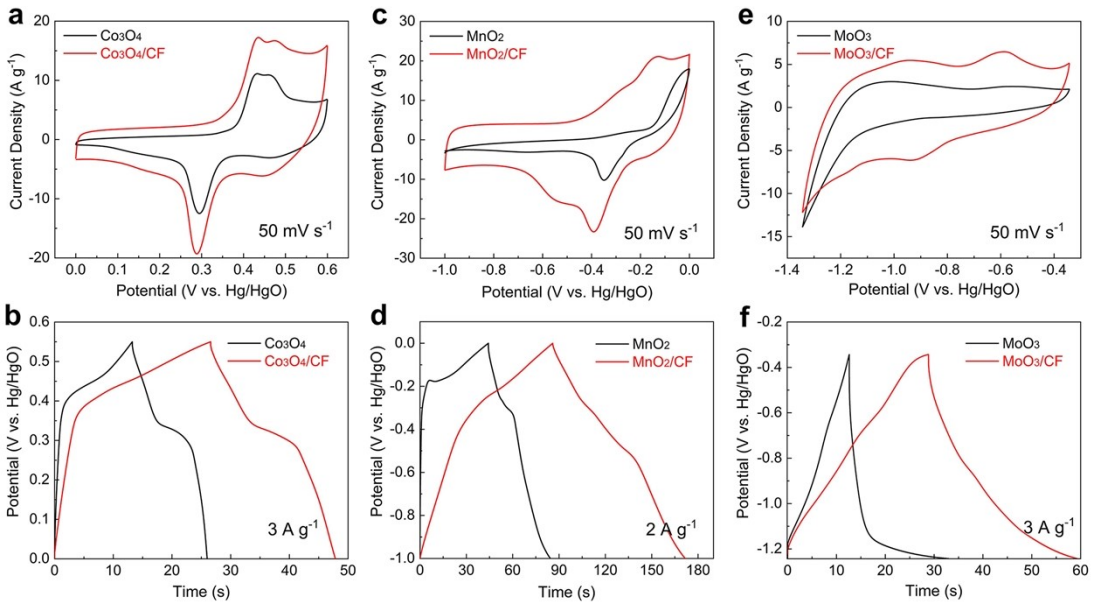

Figure S7. (a) CV curves and (b) GCD curves of Co_3O_4 and Co_3O_4/CF samples. (c) CV curves and (b) GCD curves of MnO_2 and MnO_2/CF samples. (e) CV curves and (b) GCD curves of MoO_3 and MoO_3/CF samples.

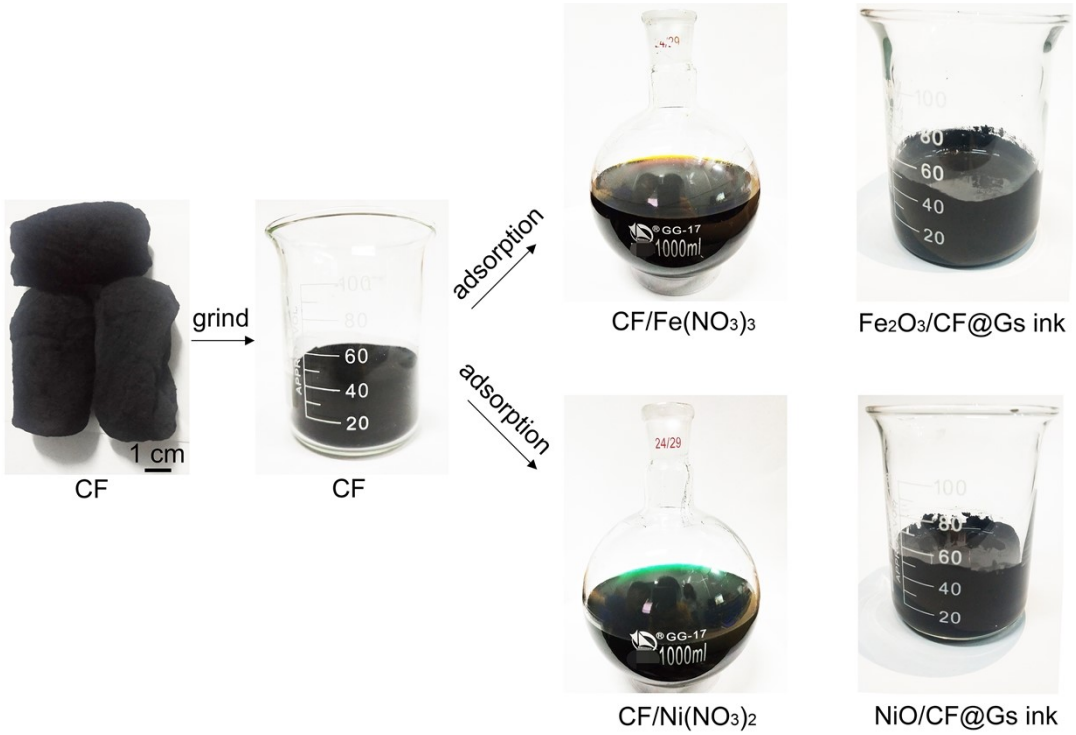

Figure S8. The large-scale fabrication of Fe_2O_3/CF@Gs and NiO/CF@Gs based inks.

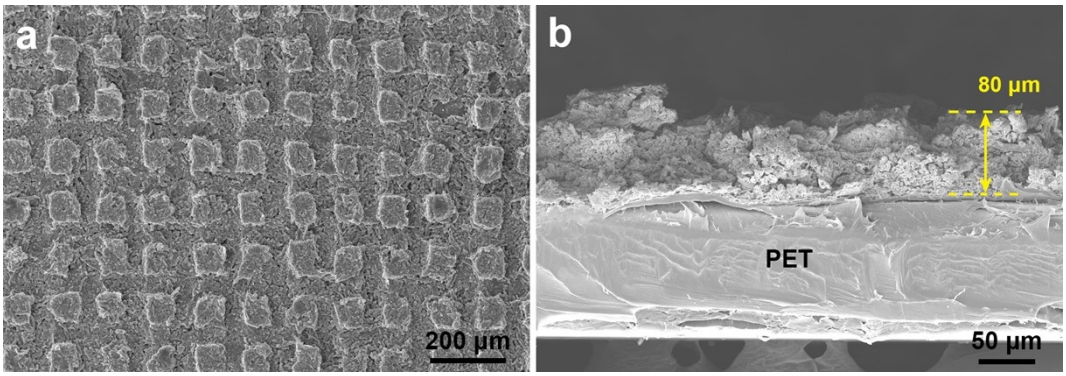

Figure S9. (a) Top-view and (b) side-view SEM images of screen-printed multi-conductive electrodes on PET substrates.

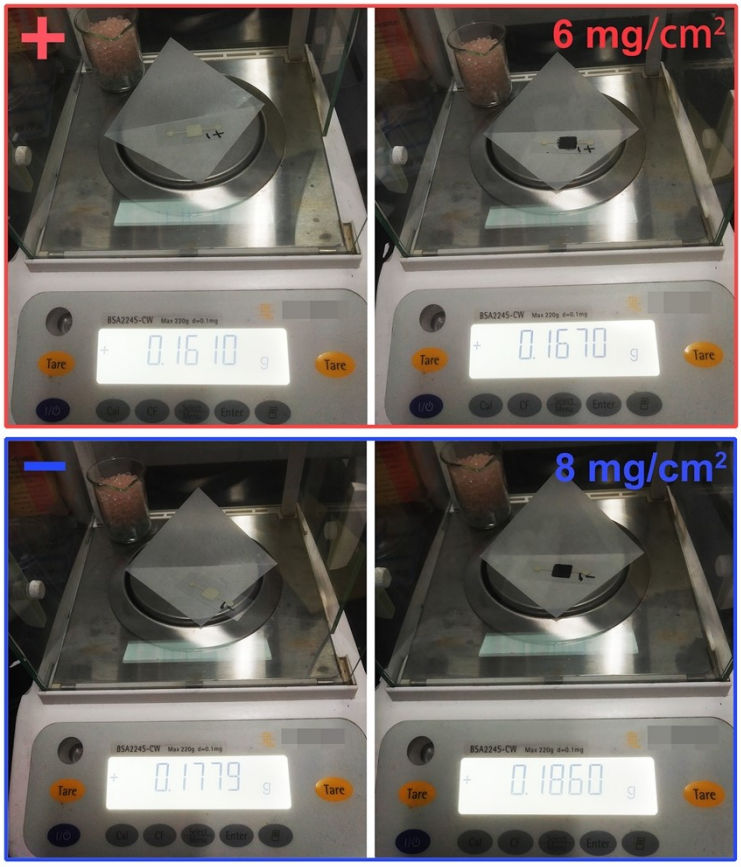

Figure S10. The weight of screen-printed positive and negative electrodes on PET substrates.

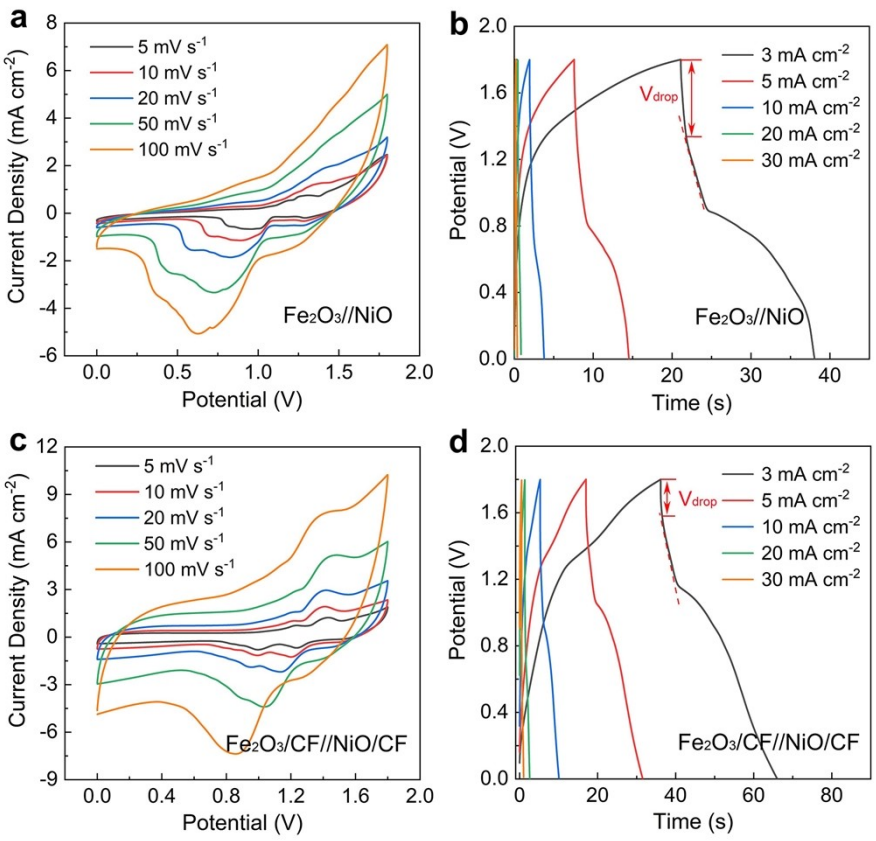

Figure S11. (a) CV and (b) GCD curves of Fe_2O_3//NiO based supercapacitors at different scan rates and current densities. (c) CV and (d) GCD curves of Fe_2O_3/CF//NiO/CF based supercapacitors at different scan rates and current densities.

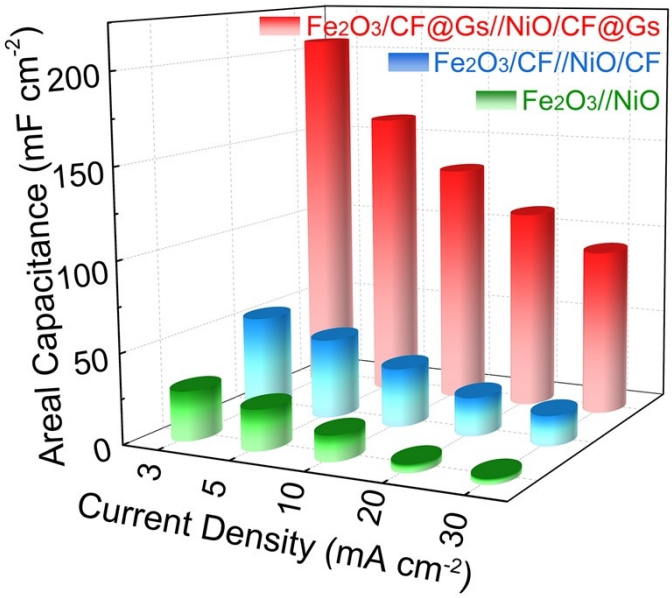

Figure S12. Areal capacitances of the Fe_2O_3//NiO, Fe_2O_3/CF//NiO/CF and Fe_2O_3/CF@Gs//NiO/CF@Gs supercapacitors at different current densities.

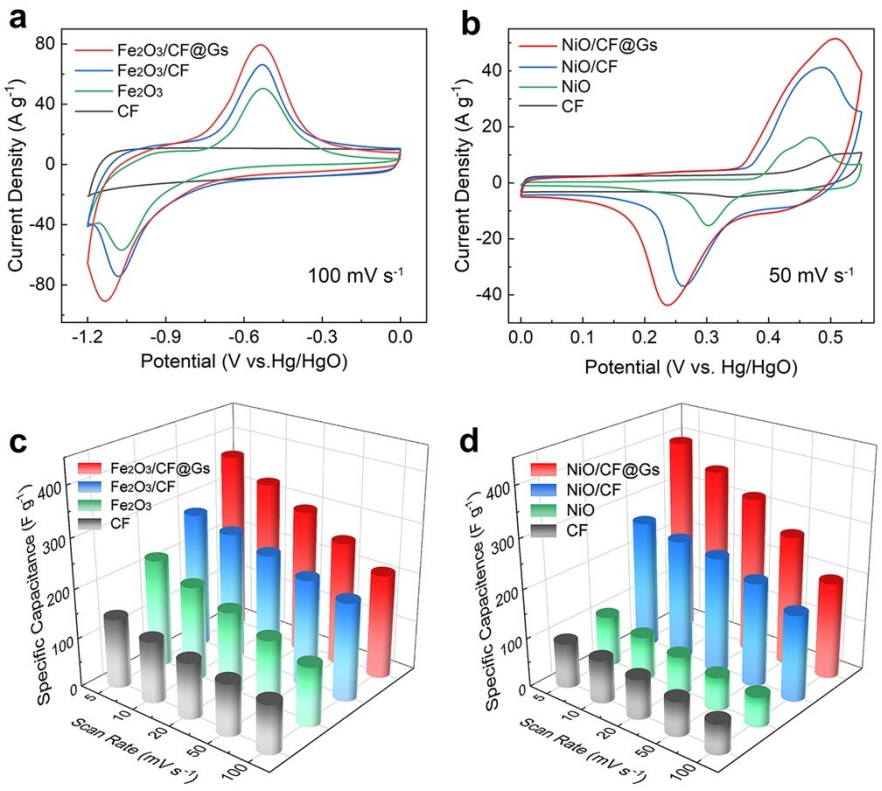

Figure S13. (a) CV curves of CF, Fe_2O_3, Fe_2O_3/CF, and Fe_2O_3/CF@Gs negative electrodes at different scan rates. (b) CV curves of CF, NiO, NiO/CF, and NiO/CF@Gs positive electrodes at different scan rates. (c) Specific capacitance of negative electrodes and (d) positive electrodes at various scan rates. Both positive and negative electrodes are with active material loading of about 2 mg on foamed nickel, details see Experimental Section.

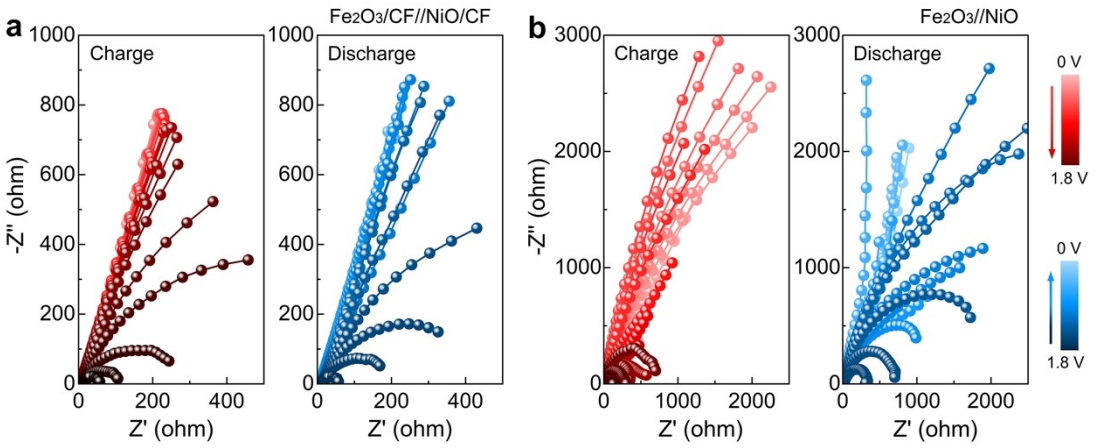

Figure S14. In-situ Nyquist plots of (a) Fe_2O_3/CF//NiO/CF and (b) Fe_2O_3//NiO based asymmetric supercapacitor at various states in charging and discharging stage.

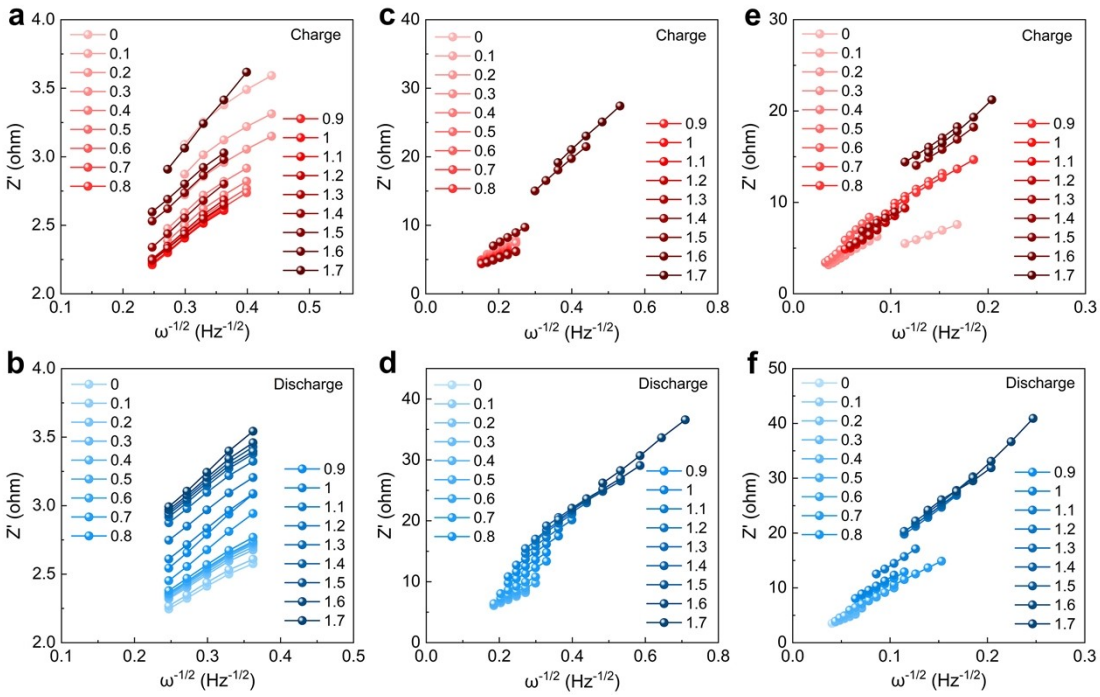

Figure S15. Real part of impedance versus $\omega^{-1/2}$ during charging and discharging stage for (a, b) Fe_2O_3/CF@Gs//NiO/CF@Gs, (c, d) Fe_2O_3/CF//NiO/CF and (e, f) Fe_2O_3//NiO based supercapacitors. The slopes determine the diffusion coefficient of ion.

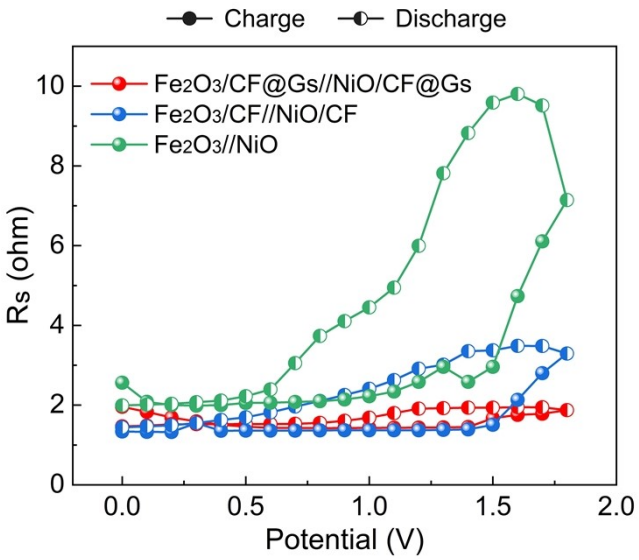

Figure S16. The equivalent series resistance (R_s) as a function of state during charging and discharging process for the Fe_2O_3//NiO, Fe_2O_3/CF//NiO/CF, and Fe_2O_3/CF@Gs//NiO/CF@Gs supercapacitors.

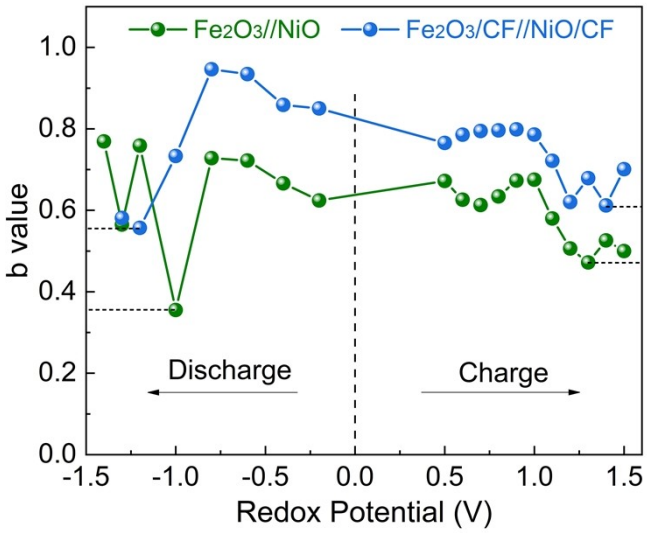

Figure S17. The *b*-values of Fe_2O_3//NiO and Fe_2O_3/CF//NiO/CF based asymmetric supercapacitors at anodic scans (charge) and cathodic scans (discharge).

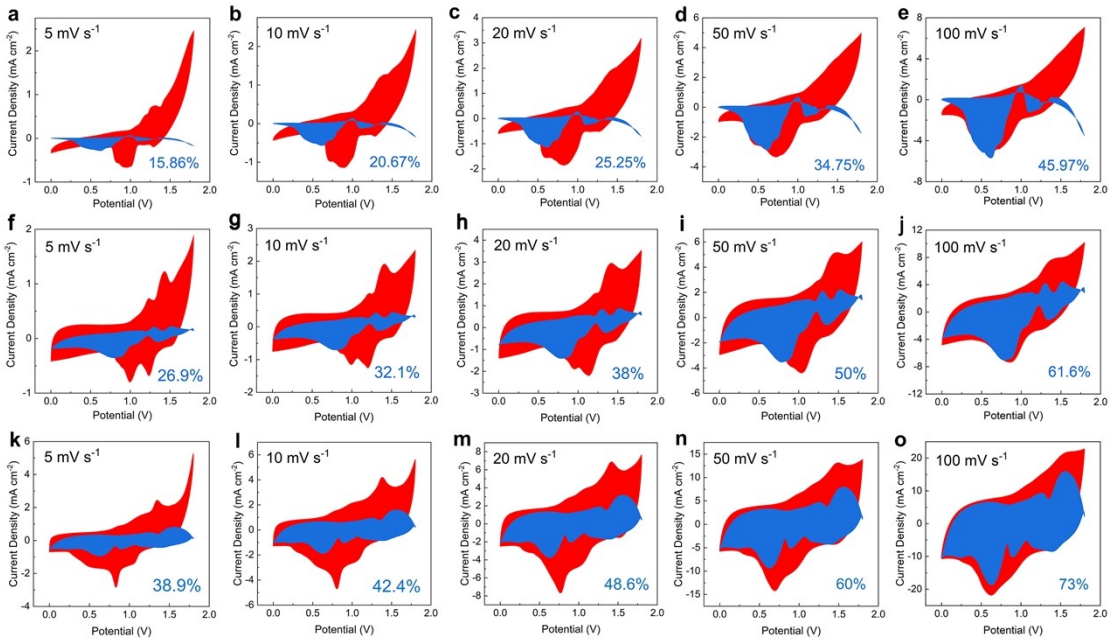

Figure S18. Separation of the surface and diffusion currents in (a-e) Fe_2O_3//NiO, (f-j) Fe_2O_3/CF//NiO/CF, and (k-o) Fe_2O_3/CF@Gs//NiO/CF@Gs based supercapacitors at various scan rates.

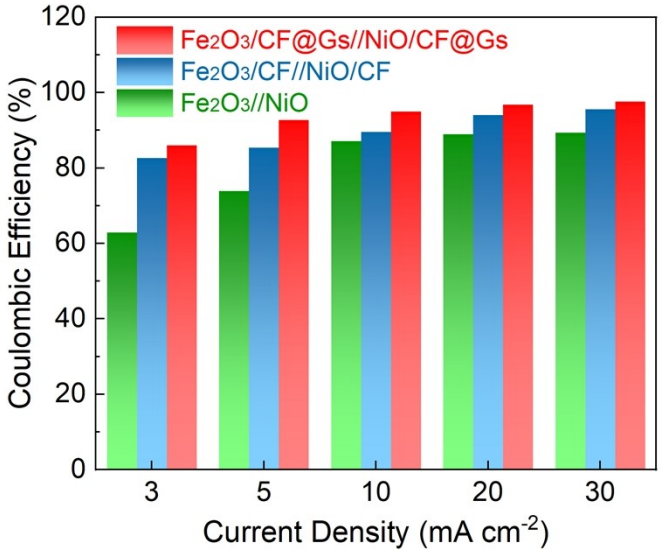

Figure S19. Coulombic efficiency of Fe_2O_3//NiO, Fe_2O_3/CF//NiO/CF and Fe_2O_3/CF@Gs//NiO/CF@Gs based supercapacitor at different current densities.

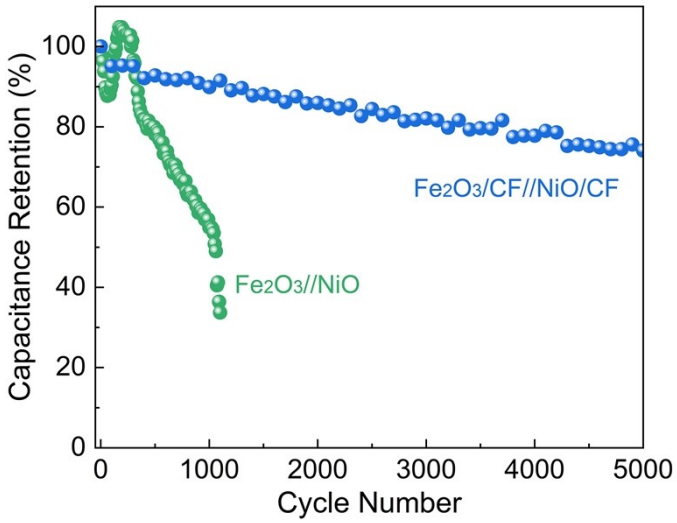

Figure S20. Capacitance retention of Fe_2O_3//NiO and Fe_2O_3/CF//NiO/CF based supercapacitor at the current density of 10 mA cm^{-2}.

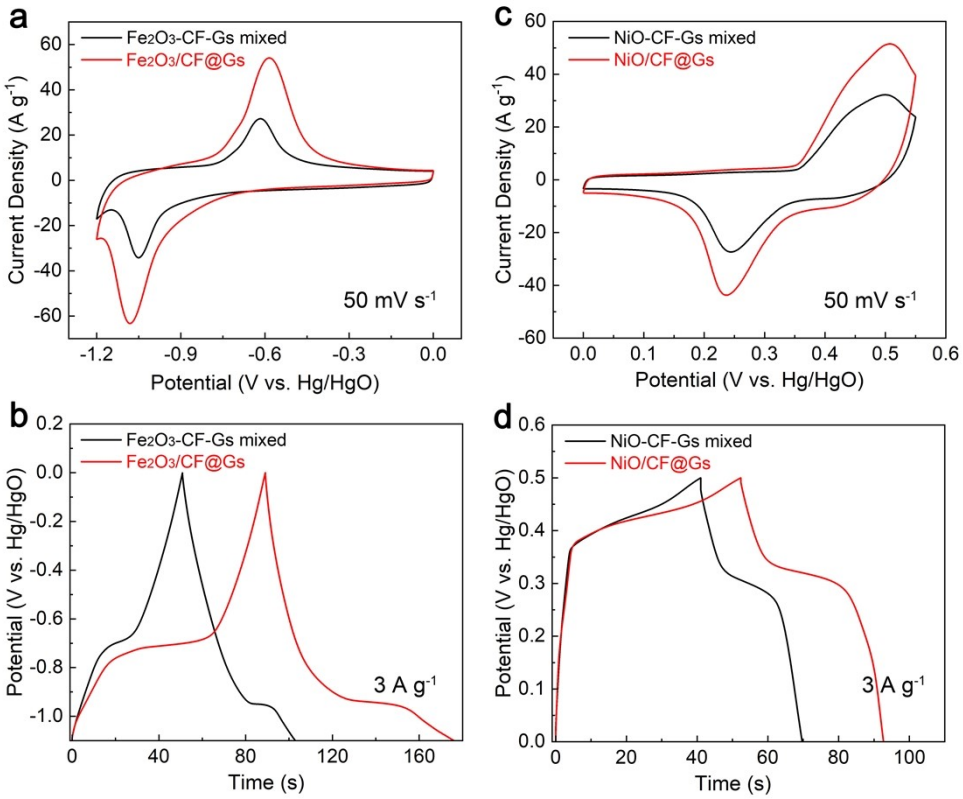

Figure S21. (a) CV and (b) GCD curves of Fe_2O_3/CF@Gs and simple physical mixed negative electrode (Fe_2O_3-CF-Gs). (c) CV and (d) GCD curves of NiO/CF@Gs and simple physical mixed positive electrode (NiO-CF-Gs).

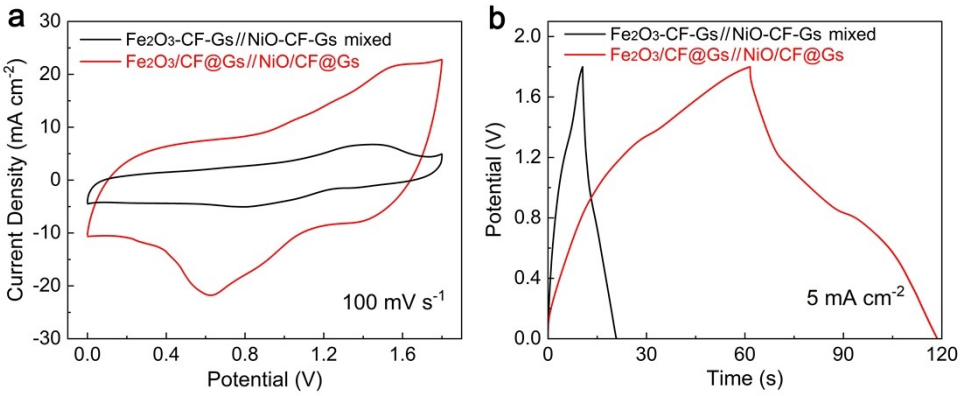

Figure S22. (a) CV curves and (b) GCD curves of Fe_2O_3/CF@Gs//NiO/CF@Gs and Fe_2O_3-CF-Gs//NiO-CF-Gs based asymmetric supercapacitors.

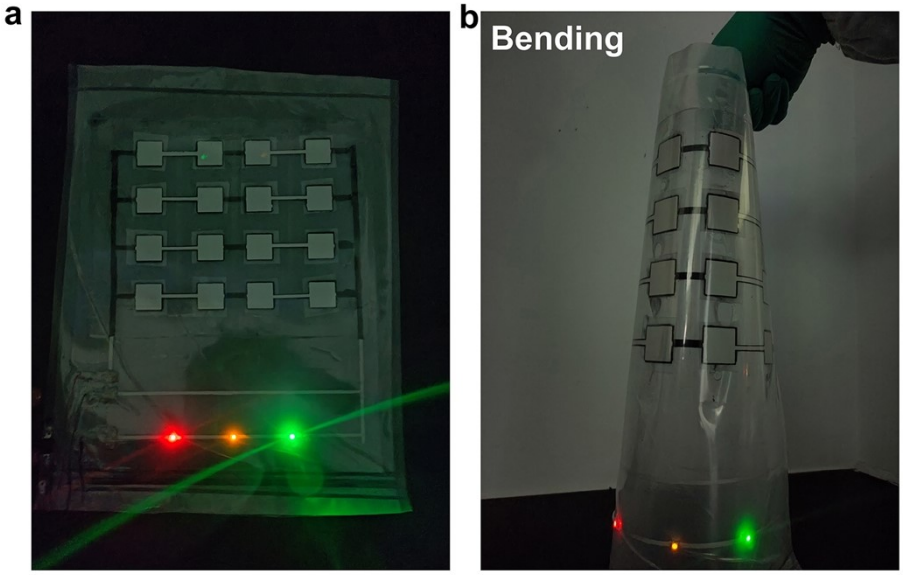

Figure S23. (a) The screen-printed 4×4 integrated Fe_2O_3/CF@Gs//NiO/CF@Gs based flexible supercapacitors and (b) under bending state to light up a 5.9 V LEDs array (1.8 V for red LED, 1.8 V for yellow LED, and 2.3 V for green LED).

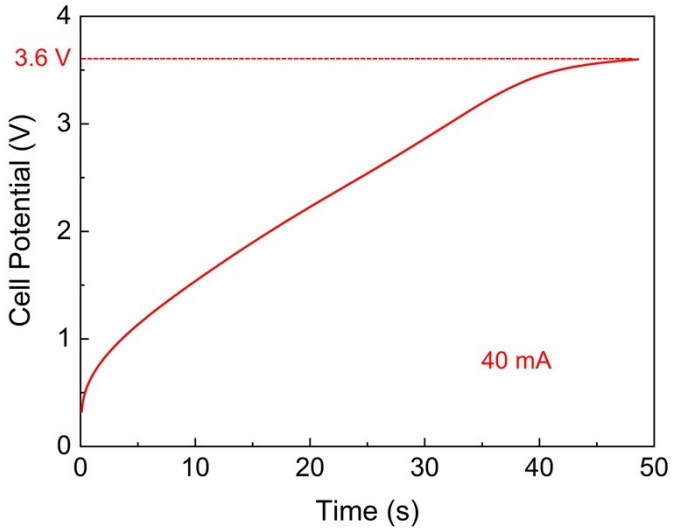

Figure S24. Constant-current charge curve of two Fe_2O_3/CF@Gs//NiO/CF@Gs based supercapacitors connected in series at 40 mA, and then power for the electronic timer.

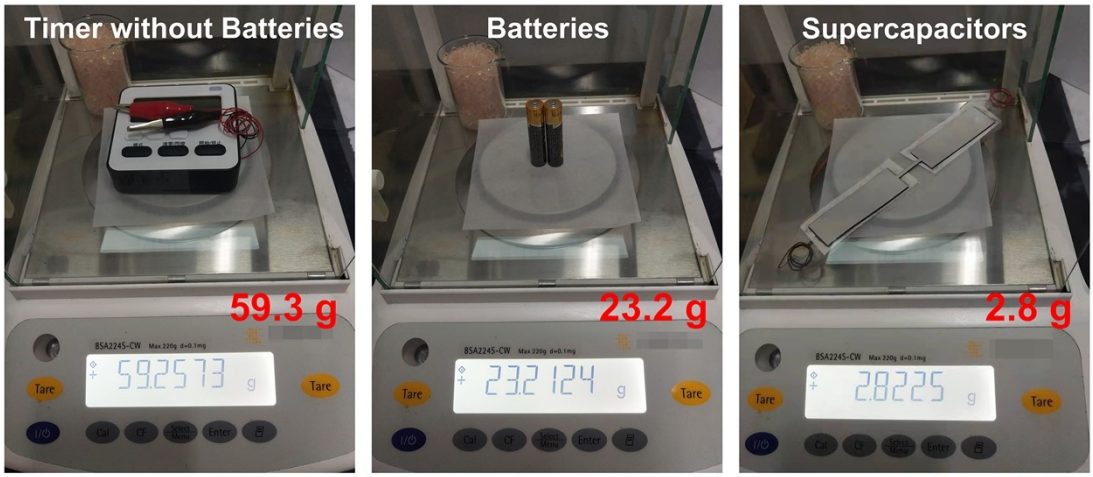

Figure S25. The weight of electronic timer without batteries, two batteries, and the printed supercapacitors.

Table S1. Adsorption parameters of different samples calculated from N_2 adsorption isotherms.

Sample	SSA ($m^2\ g^{-1}$)[a]	Total pore volume ($cm^3\ g^{-1}$)[b]	Micropore volume ($cm^3\ g^{-1}$)[c]	V_{micro}/V_{total}	Mesopore volume ($cm^3\ g^{-1}$)[d]	V_{meso}/V_{total}	Pore diameter (nm)[e]
CF	863.7	0.67	0.33	49.3%	0.34	50.7%	2.056
Fe_2O_3/CF	544.7	0.49	0.12	24.5%	0.37	75.5%	2.585
NiO/CF	526.5	0.42	0.19	45.2%	0.23	54.8%	2.63

[a]Specific surface area is calculated from the BET equation. [b]Total pore volume, [c]micropore volume (<2 nm), and [d]mesopore volume (>2 nm) calculated by Density Functional Theory (DFT). [e]Pore diameter (nm, most probable pore diameter) calculated by using the Nonlinear Density Functional Theory (NLDFT).

Table S2. The performance of Fe_2O_3/CF@Gs//NiO/CF@Gs based aqueous flexible supercapacitor compared with other recent reported flexible supercapacitors.

Type of supercapacitor	Electrolyte	Potential range (V)	Areal capacitance (mF cm^{-2})	Energy density (mW h cm^{-2})	Power density (mW cm^{-2})	Reference
Fe_2O_3/CF@Gs // NiO/CF@Gs*	**KOH/PVA**	**0-1.8**	**206.2 mF cm^{-2} at 3 mA cm^{-2}**	**0.0930**	**30**	**This work**
TSBL-MQD/LRGO	H_2SO_4/PVA	0-1.2	10.4 mF cm^{-2} at 0.6 mA cm^{-2}	0.0020	0.13	4
MnO_2@C // VN*	$MgSO_4$/PAM	0-2.2	28.5 mF cm^{-2} at 0.5 mA cm^{-2}	0.0190	23	5
CoNiP@NiOOH // ZIF-C*	KOH/PVA	0-1.4	54.7 mF cm^{-2} at 0.5 mA cm^{-2}	0.0140	6	6
p-Mn_3O_4@C*	Na_2SO_4/CMC	0-1.3	30.1 mF cm^{-2} at 0.2 mA cm^{-2}	0.0071	1.3	7
VO_x/rGO // G-VNQDs/rGO*	LiCl/PVA	0-1.6	207.9 mF cm^{-2} at 0.63 mA cm^{-2}	0.0740	3.8	8
MoO_x//MoO_x	Sodium alginate (Alg-Na)	0-1.0	112.5 mF cm^{-2} at 1 mA cm^{-2}	0.0160	2.53	9
Ex-$Ti_3C_2T_x$ //MoS_{3-x}@3DnCF*	H_2SO_4/PVA	0-1.6	160 mF cm^{-2} at 0.25 mA cm^{-2}	0.0570	10	10
MnHCF-MnO_x/ErGO*	LiCl/PVA	0-1	16.8 mF cm^{-2} at 0.1 mA cm^{-2}	0.0023	0.5	11
MoS_2/rGO//CNT*	H_2SO_4/PVA	0-1	13.7 mF cm^{-2} at 0.1 mA cm^{-2}	0.0019	1	12
$W_{18}O_{49}$ NWs/rGO	$AlCl_3$	0-1.1	48 mF cm^{-2} at 2 mA cm^{-2}	0.0052	2.2	13
MgO@G//MgO@G*	KOH/PVA	0-1.4	21.7 mF cm^{-2} at 0.5 mA cm^{-2}	0.0059	6	14

Annotation: * denotes all-printed flexible supercapacitors.

Reference

[1] Y. Feng, L. Liu, J. Liang, W. Yao, B. Tian, C. Jiang, W. Wu, *J. Power Sources* 2019, **433**, 126676.

[2] Q. Lu, L. Liu, S. Yang, J. Liu, Q. Tian, W. Yao, Q. Xue, M. Li, W. Wu, *J. Power Sources* 2017, **361**, 31-38.

[3] J. Liang, Y. Feng, L. Liu, S. Q. Li, C. Z. Jiang, W. Wu, *J. Mater. Chem. A* 2019, **7**, 15960-15968.

[4] Y. Yuan, L. Jiang, X. Li, P. Zuo, X. Zhang, Y. Lian, Y. Ma, M. Liang, Y. Zhao, L. Qu, *Adv. Mater.* 2022, **34**, e2110013.

[5] Z. Tian, X. Tong, G. Sheng, Y. Shao, L. Yu, V. Tung, J. Sun, R. B. Kaner, Z. Liu, *Nat. Commun.* 2019, **10**, 4913.

[6] M. Qiu, P. Sun, G. Cui, Y. Tong, W. Mai, *ACS Nano* 2019, **13**, 8246-8255.

[7] Z. Peng, J. Huang, Q. He, L. Tan, Y. Chen, *J. Mater. Chem. A* 2021, **9**, 4273-4280.

[8] K. Shen, J. Ding, S. Yang, *Adv. Energy Mater.* 2018, **8**, 1800408.

[9] H. Sheng, J. Zhou, B. Li, Y. He, X. Zhang, J. Liang, J. Zhou, Q. Su, E. Xie, W. Lan, K. Wang, C. Yu, *Sci. Adv.* 2021, **7**, eabe3097.

[10] K. Ghosh, M. Pumera, *Small Methods* 2021, **5**, e2100451.

[11] J. Liang, B. Tian, S. Li, C. Jiang, W. Wu, *Adv. Energy Mater.* 2020, **10**, 2000022.

[12] W. Yang, L. He, X. Tian, M. Yan, H. Yuan, X. Liao, J. Meng, Z. Hao, L. Mai, *Small* 2017, **13**, 1700639.

[13] M. Hassan, G. Abbas, Y. Lu, Z. Wang, Z. Peng, *J. Mater. Chem. A* 2022, **10**, 4870-4880.

[14] F. Li, J. Qu, Y. Li, J. Wang, M. Zhu, L. Liu, J. Ge, S. Duan, T. Li, V. K. Bandari,

M. Huang, F. Zhu, O. G. Schmidt, *Adv. Sci.* 2020, **7**, 2001561.